

JGR Solid Earth

RESEARCH ARTICLE

10.1029/2024JB030790

Key Points:

- Iron-rich lizardite is replaced by iron-poor chrysotile in highly deformed serpentinite shear zones within a transform fault zone
- Magnetite forms using iron from serpentinite replacement, implying remagnetization within deformed serpentinite due to high fluid-rock ratios
- Remagnetized serpentinite records tectonic history, including transform-related 90° rotations in the Troodos ophiolite

Correspondence to:

L. Qi,
Lqi21@imperial.ac.uk

Citation:

Qi, L., Allerton, S., Muxworthy, A. R., Zhang, Y., & Gergov, H. (2025). Remagnetization of serpentinite during deformation: Evidence from a fossil oceanic transform fault zone of the Troodos ophiolite. *Journal of Geophysical Research: Solid Earth*, 130, e2024JB030790. <https://doi.org/10.1029/2024JB030790>

Received 19 NOV 2024

Accepted 18 APR 2025

Author Contributions:

Conceptualization: Liang Qi, Simon Allerton, Adrian R. Muxworthy
Data curation: Liang Qi
Formal analysis: Liang Qi, Simon Allerton, Adrian R. Muxworthy, Hristo Gergov
Funding acquisition: Liang Qi, Adrian R. Muxworthy
Investigation: Liang Qi, Simon Allerton, Adrian R. Muxworthy, Yong Zhang
Methodology: Liang Qi, Simon Allerton, Adrian R. Muxworthy, Yong Zhang, Hristo Gergov
Project administration: Adrian R. Muxworthy
Resources: Adrian R. Muxworthy, Yong Zhang
Software: Liang Qi

© 2025. The Author(s).

This is an open access article under the terms of the [Creative Commons Attribution License](#), which permits use, distribution and reproduction in any medium, provided the original work is properly cited.

Remagnetization of Serpentinite During Deformation: Evidence From a Fossil Oceanic Transform Fault Zone of the Troodos Ophiolite

Liang Qi¹ , Simon Allerton^{2,3}, Adrian R. Muxworthy^{1,4} , Yong Zhang^{1,5} , and Hristo Gergov¹

¹Department of Earth Sciences and Engineering, Imperial College London, London, UK, ²Department of Earth Sciences, Cardiff University, Cardiff, UK, ³School of Geosciences, University of Aberdeen, Aberdeen, UK, ⁴Department of Earth Sciences, University College London, London, UK, ⁵Nanjing Institute of Geology and Palaeontology, Chinese Academy of Sciences, Nanjing, China

Abstract Serpentinization and associated chemical remagnetization of ultramafic rocks are common in tectonically active oceanic zones such as transform zones; however, it remains unclear how chemical remagnetization occurs during the deformation of serpentinite. This study aims to discuss this magnetization process with evidence from a serpentinite shear zone within the fossil transform fault of the Troodos ophiolite. We examine how serpentinite microstructures, serpentine polytypes, iron behaviors, rock magnetic properties and paleomagnetic directions evolve with increasing shearing deformation—a process that provides pathways for serpentinization fluid circulation. As serpentinite deformation increases from massive-fractured serpentinite adjacent to the shear zone to scaly and phyllonitic serpentinites within the shear zone, rock microstructure changes from unoriented mesh textures to oriented ribbon and fibrous structures. Meanwhile, the dominant serpentine mineral shifts from lizardite to chrysotile, indicating dynamic recrystallization during increasing deformation, likely resulting from elevated water/rock ratios driven by hydrothermal circulation. Rock magnetic results suggest that highly deformed scaly and phyllonitic serpentinites contain coarser magnetite grains and higher magnetite concentration compared to the less deformed massive-fractured serpentinites. These coarser magnetite grains are also attributed to higher water/rock ratios within the shear zone. More magnetite forms due to the iron released from the replacement of iron-rich lizardite by iron-poor chrysotile. The formation of magnetite records remagnetization, which helps reconstruct the deformation history of tectonically active zones. For example, paleomagnetic directions of the differentially deformed serpentinites in Troodos ophiolite indicate clockwise block rotations of up to 90°, providing evidence for dextral slip along a fossil transform fault.

Plain Language Summary Serpentinization is a hydrothermal alteration of ultramafic rocks into serpentinite, commonly found in an oceanic environment. During this alteration, magnetite forms and the associated rocks become magnetized. However, it remains unclear how magnetite forms during the increasing deformation of serpentinite in an oceanic fault zone—a process that facilitates the development of pathways for hydrothermal fluid circulation. This study investigates the mineral changes, iron behavior and magnetic properties of differentially deformed serpentinites within the fossil transform fault of the Troodos ophiolite. We observe an increasing deformation sequence of serpentinite, from less deformed massive-fractured serpentinite to intermediately deformed scaly serpentinite and highly deformed phyllonitic serpentinite. Throughout the deformation, the dominant serpentine mineral shifts from lizardite to chrysotile. Additionally, the more deformed serpentinites exhibit coarser magnetite grains and increased magnetite content compared to the less deformed serpentinites. The coarser magnetite grains are attributed to enhanced hydrothermal fluid activity in the deformed serpentinites. Magnetite formation utilizes iron released from the replacement of iron-rich lizardite by iron-poor chrysotile during the deformation of serpentinite. Paleomagnetic directions of these serpentinites show a clockwise block rotation of up to 90°, indicating dextral movement along the transform fault.

1. Introduction

Serpentinization involves hydrothermal reactions below 450°C, where olivine and pyroxene transform into serpentine, brucite and magnetite, altering paramagnetic ultramafic rocks into ferromagnetic (*s.l.*) serpentinite (Evans et al., 2013; Mével, 2003). Geological, geophysical and experimental observations indicate that serpentinite, in particular deformed serpentinite, is widespread in tectonically active settings, for example, subduction

Supervision: Simon Allerton, Adrian R. Muxworthy
Validation: Liang Qi, Simon Allerton
Visualization: Liang Qi, Hristo Gergov
Writing – original draft: Liang Qi
Writing – review & editing: Liang Qi, Simon Allerton, Adrian R. Muxworthy, Yong Zhang

mantle wedge zones, lithospheric strike-slip faults, oceanic detachment faults and transform faults (Guillot et al., 2015; Klein et al., 2022; Moore & Rymer, 2007). Furthermore, serpentinite-associated chemical remagnetization has long been suggested as a potential source of magnetic anomalies (e.g., Dymant & Arkani-Hamed, 1995), such as positive anomalies along the fracture zone of the western central Atlantic (e.g., Davy et al., 2020) and the detachment faults near 30°N Mid-Atlantic ridge (e.g., Sztikar et al., 2017). Despite these studies highlighting the importance of serpentinite on magnetic anomalies, the magnetic response of serpentinite to increasing deformation in these tectonically active zones remains less constrained.

Existing magnetic studies have concentrated on the alteration process of fresh peridotite to undeformed serpentinite, exploring various factors influencing the magnetite formation, such as the serpentinization degree (S_c), temperature (T) and water/rock ratios (e.g., Frost et al., 2013; Maffione et al., 2014). These studies have shown that little magnetite forms when S_c is low, but magnetite contents increase rapidly when S_c is >75% (Maffione et al., 2014; Oufi et al., 2002). Higher $T > 200^\circ\text{C}$ and increased water/rock ratios have been suggested to facilitate the release of iron from olivine, leading to magnetite formation and iron-poor serpentine minerals (Frost et al., 2013; Klein et al., 2014). This study focuses on differentially deformed serpentinites which have been paid little attention. We investigate how the magnetic properties in particular magnetite formation respond to increasing deformation in a fossil transform fault zone of the Troodos ophiolite, the Southern Troodos Transform Fault Zone (STTFZ).

The STTFZ is in the south part of the Troodos ophiolite (Figure 1a), retaining structures from the oceanic crust formed by back-arc spreading (Schiffman et al., 1987). It has not undergone significant metamorphism and is above sea level, making it an ideal location to study the serpentinization and magnetization process associated with an oceanic transform fault (Figure 1a) (MacLeod et al., 1990; Simonian & Gass, 1978). Within the STTFZ, well-exposed serpentinite shear zones are found in the pervasively serpentinized mantle rocks (Figure 1b) (Gass et al., 1994), providing an opportunity to study both the undeformed serpentinite adjacent to the shear zones and the in-situ deformed serpentinite within the shear zones.

Here we applied a range of techniques to study the differentially deformed serpentinites, including field investigations, optical and scanning electron microscopy, confocal Raman microscopy, rock magnetism and paleomagnetism. Our results provide insights into (a) serpentine mineral alteration and iron behavior in response to increasing deformation, (b) the magnetite formation mechanism in deformed serpentinites, (c) remagnetization and (d) the deformation mechanism within the STTFZ of the Troodos ophiolite.

2. Geological Setting

The Troodos ophiolite including the STTFZ was formed at 90–92 Ma (Chen et al., 2020; Mukasa & Luden, 1987), in a supra-subduction zone where the African plate was subducting below the Eurasian plate (Moores & Vine, 1971; Pearce et al., 1984). It experienced a $\sim 90^\circ$ anticlockwise rotation since its formation, with the Troodos mean vector (TMV) declination (D) = 274° , inclination (I) = 36° , α_{95} = 12.3° , as documented in the Turonian pillow lavas (Clube et al., 1985; Morris, 1996). This ophiolite is considered one of the most complete ophiolites worldwide and preserves a ridge-transform intersection, including the Solea spreading axis in the central part and the STTFZ in the southern part (Figure 1a) (e.g., MacLeod et al., 1990; Morris & Maffione, 2016). This study focuses on the STTFZ.

The STTFZ is delineated in the north by the Arakapas transform fault and in the south by the Anti-Troodos microplate (Figure 1b) (MacLeod & Murton, 1993). It spans over 60 km from west to east, with an exposed thickness exceeding 5 km (Gass et al., 1994). The STTFZ consists of two distinct rock sequences: (a) the transform rock sequence, ranging from greenschist facies volcanic rocks, dikes and gabbro to serpentinized ultramafic rocks; (b) the deformation rock sequence, including lava breccia, dike and gabbro clasts, syn-transform plutonic mafic and ultramafic rocks such as gabbro/wehrlite intrusions, and serpentinite, particularly serpentinite shear zones. A mutually cross-cutting relationship between these two sequences is observed, suggesting a trans-tensional transform fault zone (MacLeod & Murton, 1993; Murton, 1986).

Transform-associated deformation and kinematics are nearly east-west (E-W) (Figure 1b) (Gass et al., 1994). Most studies suggest that the STTFZ is dextral (Allerton & Vine, 1991; Bonhommet et al., 1988; Morris et al., 1990), rather than sinistral (Murton, 1986; Varga & Moores, 1985). For example, Morris et al. (1990) proposed that a clockwise rotation of up to 45° relative to the TMV occurred within 15 million years, providing evidence for dextral

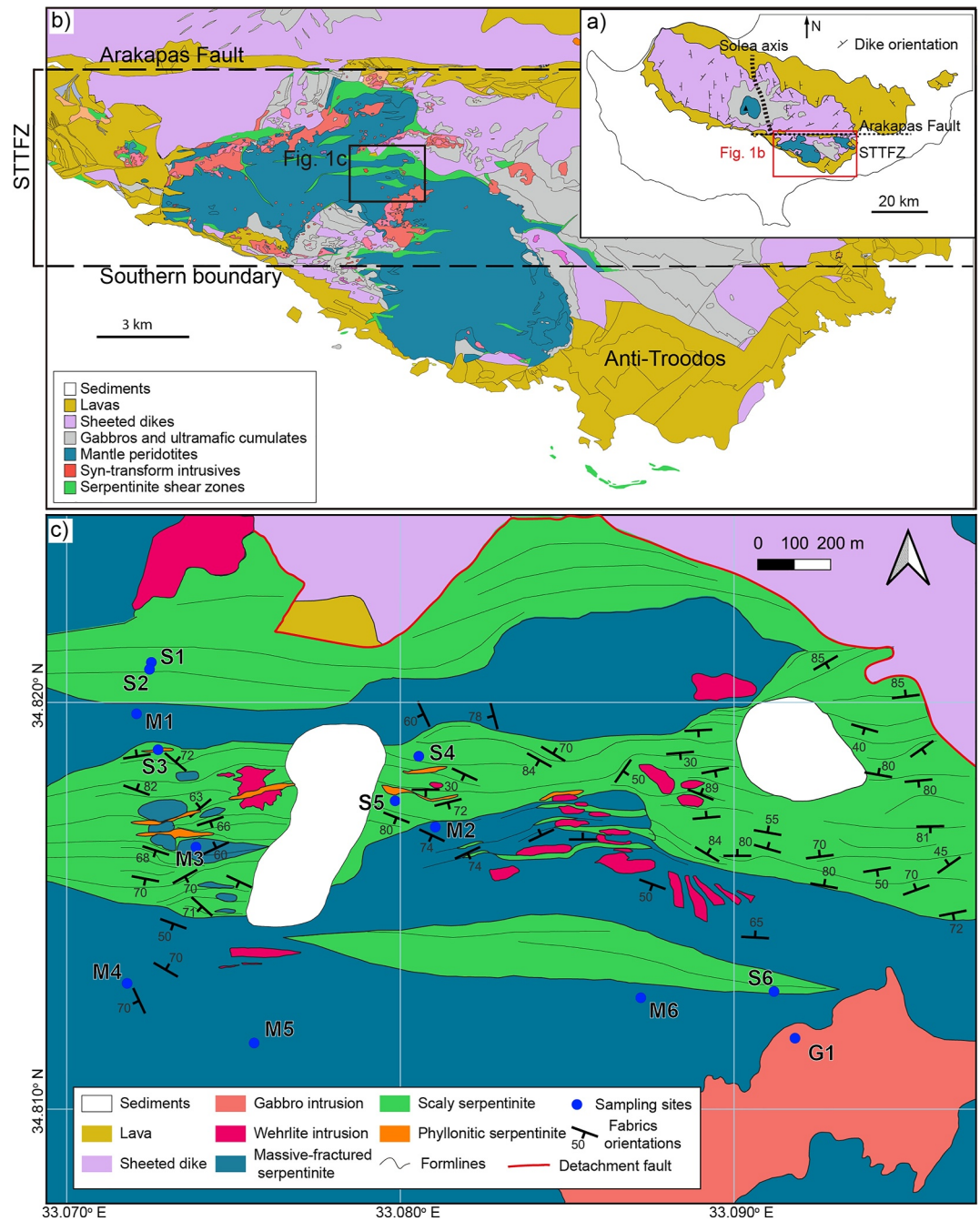


Figure 1. (a) Map of the Troodos ophiolite showing the location of the STTFZ (modified from Cox et al., 2021). A red box outlines the area shown in Figure 1b. (b) Geological map of the STTFZ highlighting serpentinite shear zones (modified from Gass et al., 1994). A black box indicates the Dheriona shear zone. (c) Detailed map of the Dheriona shear zone with fabric orientation data based on our field observations and Cox et al. (2021), showing the sampling sites of this study.

slip along the boundary of the STTFZ. Despite this, there is no clear understanding of how the inner blocks deformed within the STTFZ. Here, we study the mantle serpentinite section, near the center of the STTFZ (Figure 1b).

The STTFZ mantle rocks are pervasively serpentinized and characterized by serpentinite shear zones that extend several kilometers deep (Cox et al., 2021). These shear zones are deformation-concentrating and ideal for recovering the complex deformation history of the STTFZ. Serpentinites undergo increasing deformation as they approach the shear zones (Cox et al., 2021; MacLeod & Murton, 1995). Many of the shear zones also contain

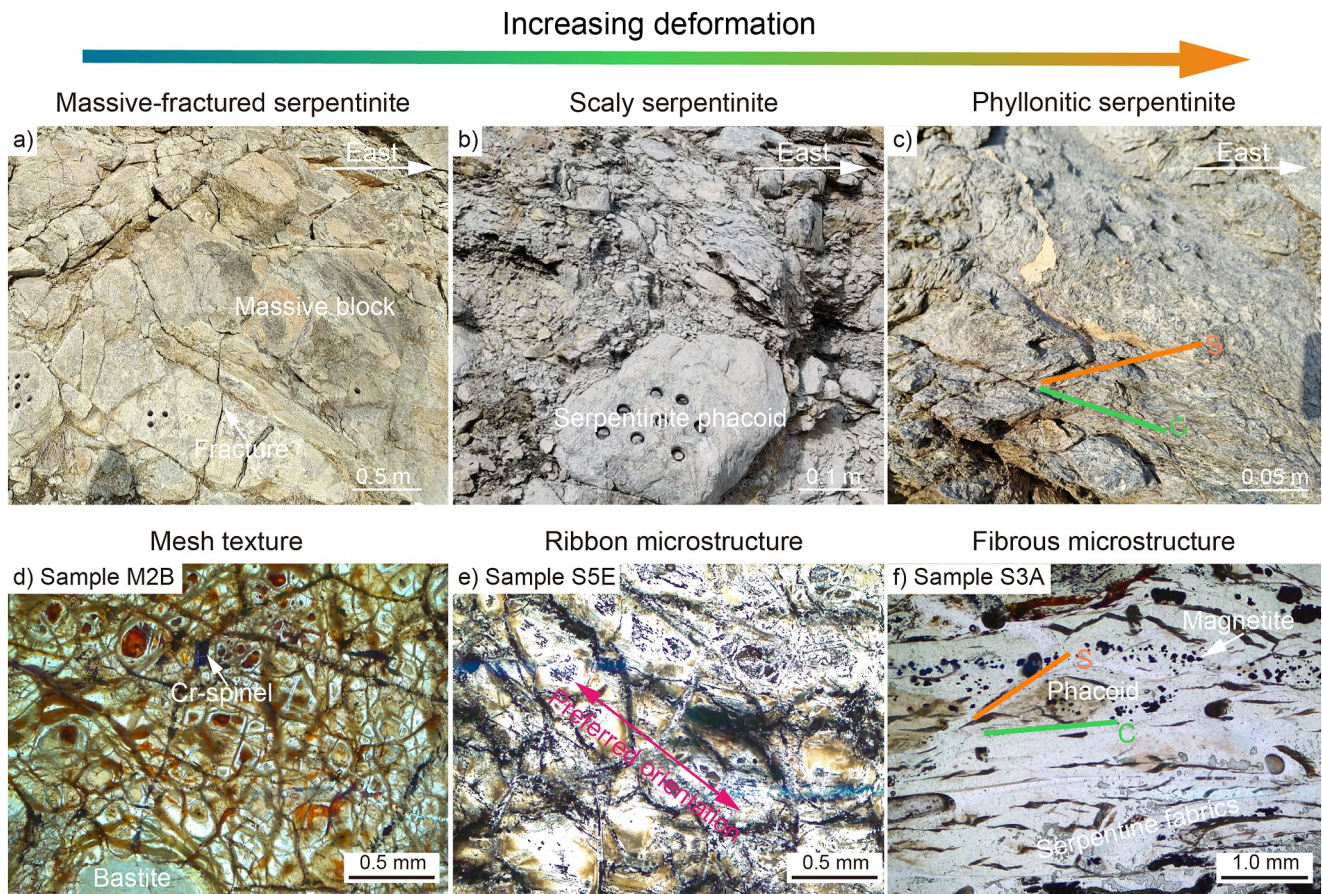


Figure 2. (a), (b), and (c) Field photos showing the massive-fractured (near site M2), scaly (near site S5) and phyllonitic serpentinites (near site S3), respectively. (d), (e), and (f) Representative crossed polarized images for the mesh texture of sample M2B, ribbon microstructure of sample S5E and fibrous microstructure of sample S3A.

isolated wehrlite and gabbro plutons with associated dikes, which are interpreted as intrusions that occurred simultaneously with the transform-related deformation (MacLeod & Murton, 1993; Martin et al., 2023). These intrusions are suggested to provide heat for serpentinization and constrain the timing of the shear deformation (Martin et al., 2023).

Our study focuses on the Dhierona serpentinite shear zone (Figure 1c). Dominant E-W structures suggest the Dhierona shear zone formed due to transform-related shearing. Within this zone and its surrounding area, the pre-serpentinization lithology of the mantle lithosphere is primarily harzburgite, comprising more than 90% (Cox et al., 2021; Gass et al., 1994). Some dunite is observed in meter-scale pods or as massive bodies up to several hundred meters. Both harzburgite and dunite have undergone extensive serpentinization. When shearing is absent, the original lithology is usually recognizable. In harzburgite, orthopyroxene is replaced by bastite, while dunite is distinguished by the absence of bastite and a higher proportion of Cr-spinel. Notably, a kilometer-scale gabbroic intrusion, emplaced synchronously with transform faulting, is located on the southern side of the Dhierona shear zone (Gass et al., 1994).

3. Methods

3.1. Rock Descriptions and Sampling

Field mapping was conducted for the Dhierona shear zone, building on previous work by Gass et al. (1994) and Cox et al. (2021). Various field structures were observed, including brittle fractures, faults, ductile schistosité-cisaillement (S-C) structures and foliations. Based on these structures, three groups of serpentinites have been identified: (a) massive-fractured serpentinite adjacent to the shear zone, (b) scaly serpentinite and (c) phyllonitic serpentinite within the shear zone, indicating increasing deformation (Figure 2). 81 orientated samples were

collected from 13 sites, including six localities for the massive-fractured serpentinite, six localities for both the scaly and phyllonitic serpentinites and one locality for the syn-transform gabbro intrusion (Figure 1c). Sample densities (ρ) were measured to estimate S_c based on an empirical equation $S_c = [3.30 - (\rho - 5.2 \times m)/(1 - m)]/0.785 \times 100$ (Oufi et al., 2002), where m is the magnetite volume fraction, using a microbalance with a precision of 0.0001 g and the water displacement method to determine sample volumes (e.g., Miller & Christensen, 1997; Oufi et al., 2002). Given the equation used and measurement errors, the estimated S_c has an uncertainty of $\sim 10\%$ (e.g., Nuriel et al., 2009). Descriptions and imaging of rock microstructures were also conducted to explore how serpentinites accommodate increasing strain at the mineral scale using thin sections examined under an optical microscope.

3.2. Serpentine Mineral Quantification

Serpentine minerals forming various microstructures were identified and imaged using an integrated Raman and SEM (RISE) system at the Nanjing Institute of Geology and Paleontology, Chinese Academy of Sciences. The RISE system includes the Tescan MAIA-3 field emission gun SEM, equipped with Oxford Instruments X-Max 80NT SDD energy dispersive X-ray spectroscopy (EDX) for determining elemental composition. Serpentine polytypes, such as lizardite, chrysotile and antigorite, were identified using an Alpha 300R + confocal Raman microscope within the RISE system.

Ten independent areas from three rock-thin sections of representative massive-fractured, scaly and phyllonitic serpentinites were prepared to collect Raman spectroscopy data. The analysis was performed using a 100 \times dry objective (Zeiss, Oberkochen) and a 532 nm laser with a power of 50 mW, following the procedures outlined by Rooney et al. (2018). Before each session, the Raman microscope was calibrated and optimized using a silicon wafer and a powdered kaolinite sample, verifying the Si band at 520.6 cm^{-1} and the kaolinite OH band at 3,620.6 cm^{-1} . A high-resolution grating with 1,200 grooves per millimeter, centered at 3,700 cm^{-1} , was employed. Individual Raman spectra were acquired with a step size of 366 nm and an acquisition time of 2 seconds per point. Background subtraction was applied to the collected spectra, and peaks were fitted using the Gaussian-Lorentzian (Voigt) function (e.g., Yuan & Mayanovic, 2017).

3.3. Rock Magnetic Analysis

Several rock magnetism measurements were performed to quantify the impact of increasing deformation on rock magnetic properties, including magnetic mineral types, grain sizes and concentration. These measurements, along with subsequent paleomagnetism measurements were all carried out at the Natural Magnetism Laboratory, Imperial College London.

High-temperature susceptibility ($HT\text{-}\chi$) measurements were conducted using the AGICO MFK1-FA instrument to help identify magnetic minerals. Crushed rock powders ($\sim 500 \mu\text{m}$) were heated from room temperature to 700 $^\circ\text{C}$ and cooled in an argon atmosphere to prevent oxidation. Bulk magnetic susceptibility was also measured.

Magnetic grain size was analyzed through magnetic hysteresis measurements. Magnetic hysteresis loops, backfield remanence curves and first-order reversal curves (FORCs) (Roberts et al., 2000) were measured using a Princeton Measurements Corporation MicroMag 3900 vibrating-sample magnetometer, with an applied saturation field of 0.5 T. After correcting the hysteresis loops for the paramagnetic slope, hysteresis parameters, that is, saturation magnetization (M_s), saturation remanent magnetization (M_{rs}) and the coercivity (B_c) were determined. Remanent coercivity (B_{cr}) was calculated from the backfield remanence curves. $m\%$, which represents m expressed as a percentage, was estimated from the saturation magnetization parameters (Klein et al., 2014; Oufi et al., 2002), using the equation $m\% = (M_{rs}/92) \times 100$, where 92 Am^2/kg is the saturation magnetization of pure magnetite (Pauthenet & Bochirol, 1951).

3.4. Paleomagnetic Analysis

Paleomagnetic directional analysis was used to constrain the timing of serpentinization and reconstruct the potential transform-associated block rotations. Paleomagnetic cores were oriented using both a sun compass and a magnetic compass in the field. These cores were then cut into cylinders with a diameter of one inch and a length of 2.2 cm. The magnetization, including natural remanent magnetization (NRM), was measured using a Molspin spinner magnetometer in a magnetically shielded room. To identify the characteristic remanent magnetization

Table 1
Paleomagnetic Sampling Locations With Relevant Lithology Descriptions and Paleomagnetic Parameters

Sites	Type	Lithology	Lon (°N)	Lat (°E)	ρ (g/cm ³)	S_c (%)	D (°)	I (°)	α_{95} (°)	N/N_0	R	κ
M1	Massive-fractured	Harzburgite	33.07209	34.81972	2.55	96	354	-2	5	6/6	6.0	160
M2	Massive-fractured	Harzburgite	33.08105	34.81694	2.49	100	309	43	7	6/6	6.0	101
M3	Massive-fractured	Harzburgite	33.07387	34.81644	2.64	91	312	33	4	5/5	5.0	377
M4	Massive-fractured	Harzburgite	33.07181	34.81309	2.48	100	307	10	7	5/5	5.0	135
M5	Massive-fractured	Dunite	33.07562	34.81162	2.50	100	307	17	10	7/7	6.8	37
M6	Massive-fractured	Harzburgite	33.08721	34.81274	2.56	94	307	33	7	5/5	5.0	124
S1	Scaly	Harzburgite	33.07254	34.82099	2.42	100	350	36	7	6/7	5.9	87
S2	Scaly	Harzburgite	33.07248	34.82082	2.56	100	341	32	7	6/10	6.0	103
S3	Phyllonitic	Harzburgite	33.07274	34.81884	2.46	100	336	20	8	5/5	5.0	92
S4	Scaly	Harzburgite	33.08055	34.81868	2.48	100	338	30	8	5/5	5.0	89
S5	Scaly	Harzburgite	33.07985	34.81778	2.50	100	358	8	6	9/10	8.9	72
S6	Scaly	Harzburgite	33.0912	34.81289	2.60	98	332	27	8	5/5	5.0	83
G1	Intrusions	Gabbro	33.09183	34.81174	2.88	NaN	313	31	7	5/5	5.0	135

Note. Lon and Lat are the longitude and latitude; ρ is the mean density; S_c is the serpentinization degree; D and I are the declination and inclination of the site mean direction; α_{95} is the radius of 95% cone of confidence centered on the mean direction; N is the number of specimens used to determine the ChRM from a total of N_0 specimens measured; R is the resultant vector; κ is the precision parameter (Fisher, 1953). Note that S_c estimation is not applicable to gabbro. All the sampling sites are shown on Figure 1c.

(ChRM), progressive demagnetization techniques were applied, either through thermal demagnetization or alternating field (AF) demagnetization. Thermal demagnetization involved heating the rock cores in an ASC TD-48SC oven from room temperature to 600°C, with intervals of 50–100°C up to 400°C and then reduced to 30–40°C per step beyond 400°C. AF demagnetization was conducted using an AGICO LDA-3A AF demagnetizer with a peak field of 100 mT, with intervals of 2–3 mT up to 30 mT and then increasing to 5–10 mT per step beyond 30 mT. Demagnetization results were analyzed using principal component analysis (PCA) (Kirschvink, 1980), which was performed within the PuffinPlot software (Lurcock & Wilson, 2012).

4. Results

4.1. Rock Descriptions

The measured densities for the massive-fractured serpentinite range from 2.48 to 2.64 g/cm³, while the densities for the scaly and phyllonitic serpentinites are from 2.42 to 2.60 g/cm³ (Table 1). These low densities indicate $S_c > 90\%$ for mantle rocks near the Dhierona shear zone.

These variably deformed serpentinites exhibit diverse microstructures. (a) Massive-fractured serpentinite is less deformed with well-developed mesh textures, as seen in optical images (Figures 2a and 2d). (b) Scaly serpentinite is defined by serpentinite phacoids surrounded by a network of anastomosing disjunctive cleavage (Cox et al., 2021). The phacoids vary in size from several millimeters to decimeters (Figure 2b). The scaly serpentinite has ribbon microstructures, which are deformed mesh textures with one dominant rim orientation (Figure 2e). (c) Phyllonitic serpentinite features closely spaced cleavage (<2 mm) that is more planar than in scaly serpentinite, with the S and C planes effectively parallel. Serpentinite phacoids are present but isolated. Fibrous microstructures, consisting of serpentine fibers and a few rigid serpentinite clasts, are common (Figure 2f).

Magnetite minerals are observed in all samples and their distributions are controlled by the microstructures. For example, magnetite is mainly in the rims of mesh textures and serpentine veins of the ribbon and fibrous microstructures (Figure 2; Figure 3). This spatial relationship indicates that the magnetite grains formed during hydrothermal alteration and thus likely carry chemical remanent magnetization (CRM) from that period.

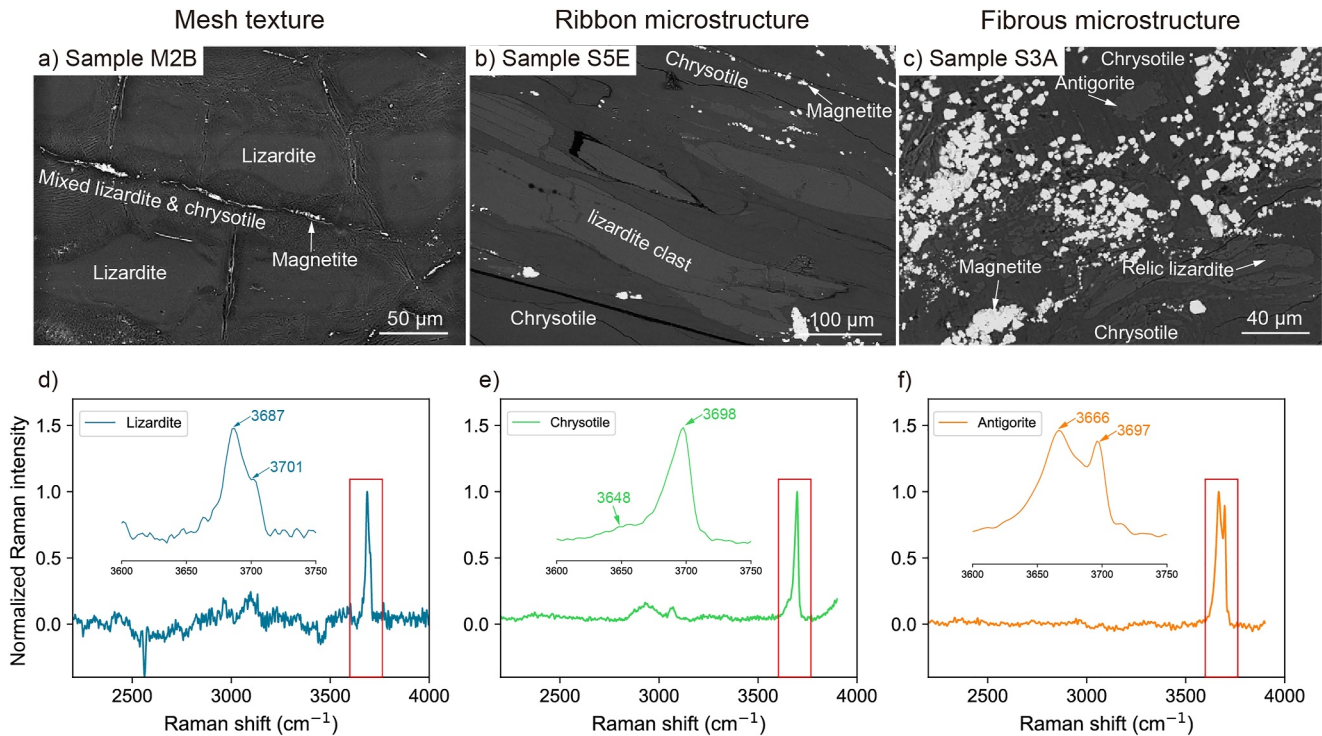


Figure 3. SEM backscatter images for serpentine minerals in different microstructures: (a) mesh texture of sample M2B, (b) ribbon microstructure of sample S5E and (c) fibrous microstructure of sample S3A. Representative Raman spectra for (d) lizardite in sample M2B, (e) chrysotile in sample S5E and (f) antigorite in sample S3A.

4.2. Serpentine Mineral Quantification

It is difficult to distinguish the serpentine minerals in the low Raman wave-number region such as 150–1,200 cm^{-1} (e.g., Rooney et al., 2018; Tarling et al., 2018). However, in the high-wavenumber region, associated with O-H stretching vibrations, the distinct band shapes have allowed for clear identification of serpentine minerals presented in this study (Figures 3d–3f). Lizardite has two dominant peaks at $3,687 \pm 2$ and a partially resolved shoulder near $3,701 \pm 5$ cm^{-1} ; chrysotile shows a main peak at $3,698 \pm 2$ cm^{-1} with a broad shoulder around $3,648 \pm 2$ cm^{-1} ; antigorite is identified by two peaks at $3,666 \pm 2$ and $3,697 \pm 2$ cm^{-1} .

The dominant serpentine minerals vary among the differently deformed serpentinites. In the massive-fractured serpentinite, lizardite is the predominant mineral, comprising over 55–60 vol%, while chrysotile makes up less than 40–45 vol%, estimated from their respective area proportions in the SEM images. Within the mesh texture, lizardite primarily forms the core, while the rim is a mixture of lizardite and chrysotile (Figure 3a). In the scaly serpentinite, chrysotile dominates, constituting more than 60 vol%, with lizardite making up less than 40 vol%. The ribbon microstructure shows an increase in chrysotile, while the deformed cores retain lizardite (Figure 3b). The phyllonitic serpentinite contains a higher proportion of chrysotile (70–90 vol%), which forms the fibrous microstructure, although relic lizardite is still present at 10–30 vol% (Figure 3c). Minor amounts of antigorite have been identified in the phyllonitic serpentinite (Figures 3c and 3f). Importantly, magnetite grains are consistently found in chrysotile zones, suggesting a close relationship between magnetite formation and chrysotile.

4.3. Rock Magnetic Analysis

$HT-\chi$ results indicate that magnetite is the primary magnetic mineral, despite the presence of other magnetic minerals such as ferritchromite, maghemite and hematite (Figures 4a–4c). During heating, a slight increase in χ between 100 and 150°C signals the presence of ferritchromite (Hodel et al., 2020). As the temperature rises, ferritchromite becomes unstable, leading to the formation of maghemite and a subsequent increase in χ . Ferritchromite forms as an intermediate product during the alteration of Cr-spinel in the process of serpentinization (Hodel et al., 2020; Yu & Tikoff, 2020). Ultimately, Cr-spinel alters into magnetite after extensive serpentinization, resulting in a weaker ferritchromite signal in the phyllonitic serpentinite compared to the massive-fractured and

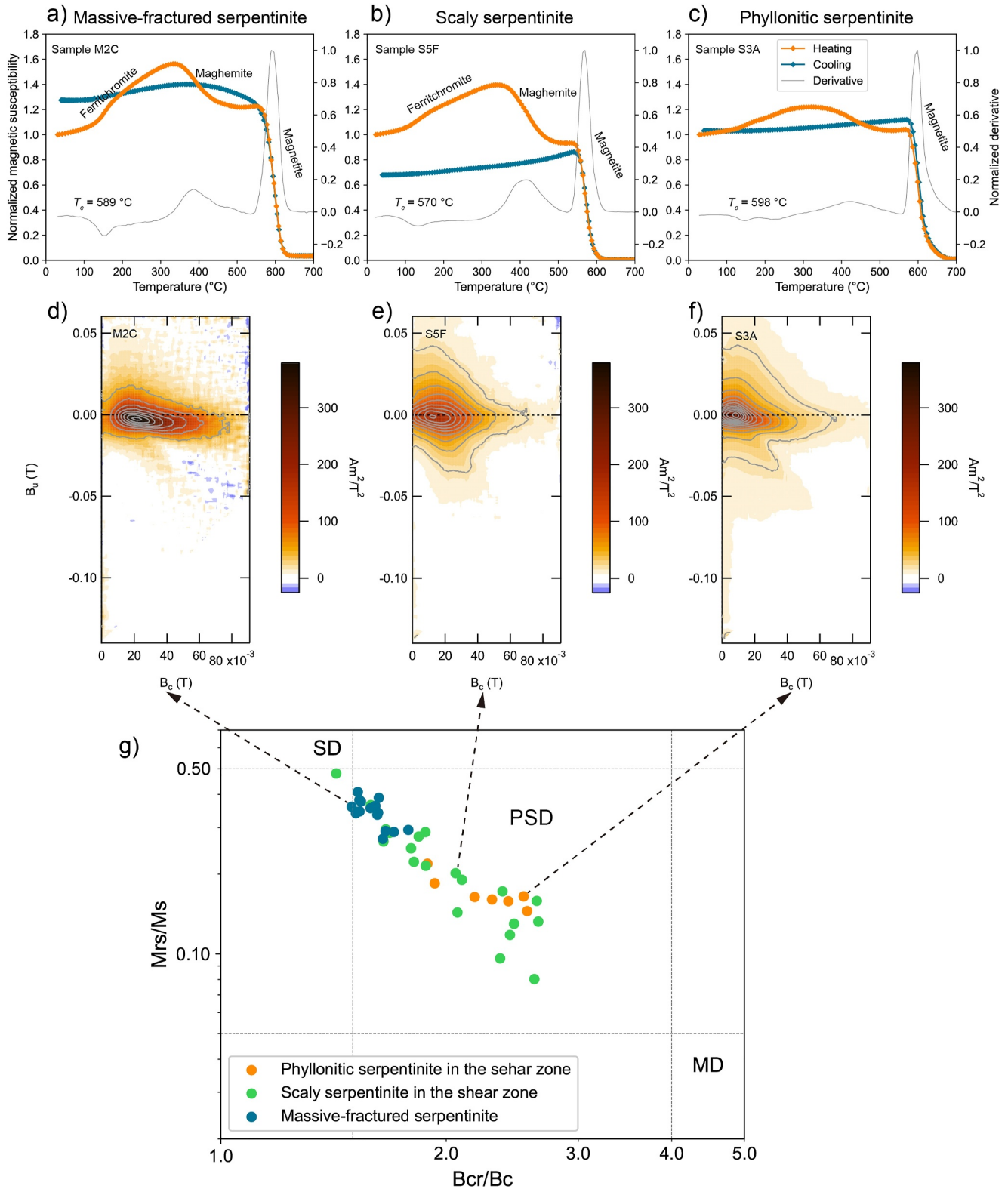


Figure 4.

scaly serpentinites (Figure 4c). Between 300 and 500°C, maghemite undergoes inversion into hematite, resulting in a decrease of χ (Muxworthy et al., 2023). At ~580°C, the dominant magnetic mineral (magnetite, >95 vol%) becomes unblocked, while a small amount of hematite ($T_c \sim 680^\circ\text{C}$) is suggested by high unblocking temperature (Figure 4c) (Dunlop & Özdemir, 2001).

All serpentinite samples have magnetic grains in the pseudo-single domain (PSD) state indicated by the Day plot (Day et al., 1977) (Figure 4g). Despite this, differences in magnetic grain size are observed in the differentially deformed serpentinites. For example, the massive-fractured serpentinite displays higher M_{rs}/M_s and lower B_{cr}/B_c values compared to the scaly and phyllonitic serpentinites, implying more single domain (SD)-like behavior and smaller magnetic grain sizes. In contrast, the phyllonitic serpentinite generally shows lower M_{rs}/M_s values, indicating coarser magnetic mineral grains.

FORC distributions show peaks between 20 and 30 mT and spreading along the B_c axis is related to the SD or single vortex particles (Nagy et al., 2024), indicating high coercivity values for the massive-fractured serpentinite (Figure 4d). The divergence of contour lines that spread out along the B_u axis is due to the PSD or multi-domain (MD) grains in the scaly and phyllonitic serpentinites (Figures 4e and 4f) (e.g., Nagy et al., 2024; Roberts et al., 2014). Overall, the hysteresis results, including the hysteresis parameters and FORCs, suggest the massive-fractured serpentinite shows more SD-like behavior, while the scaly and phyllonitic serpentinites exhibit more MD-like behavior.

4.4. Magnetic Susceptibility, NRM and Magnetite Concentration

Scaly and phyllonitic serpentinites demonstrate higher magnetic susceptibility values with a log-normal mean value of $53 \pm 1 \times 10^{-3}$ SI, compared to the massive-fractured serpentinite mean of $29 \pm 1 \times 10^{-3}$ SI (Figure 5). For the NRM, both the massive-fractured and scaly serpentinites have a wide range from 1.5 to 9.0 A/m. In contrast, the phyllonitic serpentinite shows slightly lower but more consistent NRM values, ranging from 3.0 to 4.0 A/m. Meanwhile, all these serpentinite specimens have Königsberg ratios (Q) > 1, that is, the NRM greater than induced magnetization (Figure 5a). Some massive-fractured serpentinite specimens can have high $Q > 5$; the phyllonitic serpentinite samples generally show $Q < 2$.

Higher magnetite concentrations are found in the deformed serpentinite compared to the less deformed serpentinite (Figure 5b). The massive-fractured serpentinite has magnetite contents with a mean value of $2.0 \pm 0.7\%$. In contrast, the scaly and phyllonitic serpentinites have higher mean values of $4.0 \pm 2.3\%$ and $4.6 \pm 1.7\%$, respectively. Our results suggest that both magnetic susceptibility and magnetite concentration enhance within the shear zone, implying a magnetite formation process with increasing deformation in a transform fault zone.

4.5. Paleomagnetic Analysis

Out of 81 cores, 75 give stable characterized remanent magnetization (ChRM) from 13 localities, including differentially deformed serpentinites and gabbros (Figure 6). Orthogonal projection plots of demagnetization data are typically characterized by a single stable component, despite unstable viscosity remanent magnetization below 100–250°C or 2–5 mT (Figures 6a–6c). The serpentinite specimens were demagnetized gradually, with over 70% of the magnetization demagnetized at <450°C, that is, unblocking <450°C (Figures 6a and 6b). In contrast, the gabbro samples were not significantly demagnetized below 500–550°C, indicating a higher unblocking temperature between 550 and 580°C (Figure 6c). Given their similar magnetic grain size distributions, the differences in unblocking temperatures suggest that the serpentinites carry chemical remanent magnetization (CRM) linked to serpentinitization, while the gabbro exhibits a primary thermal remanent magnetization (TRM). The CRM-carrying magnetite formed through low-temperature hydrothermal processes ($T < 450^\circ\text{C}$) is often nonstoichiometric, containing cation vacancies or partial oxidation toward maghemite-like structures (e.g., Dunlop & Özdemir, 2001).

Figure 4. (a), (b) and (c) HT- χ curves for massive-fractured sample M2C, scaly sample S5F and phyllonitic sample S3A, respectively. Susceptibility data are normalized by susceptibility values at room temperature. The maximum values of the first-order derivative curves are used to estimate the Curie temperature (T_c). (d), (e) and (f) Representative FORC diagrams for massive-fractured sample M2C, scaly sample S5F and phyllonitic serpentinite sample S3A. FORCs were processed using FORCinel 3.0 with a smooth factor of 5 (Harrison & Feinberg, 2008). (g) Day plot for specimens of different serpentinites, delineating magnetic domain states of specific grain sizes into distinct areas, including the SD, PSD and MD states (Day et al., 1977).

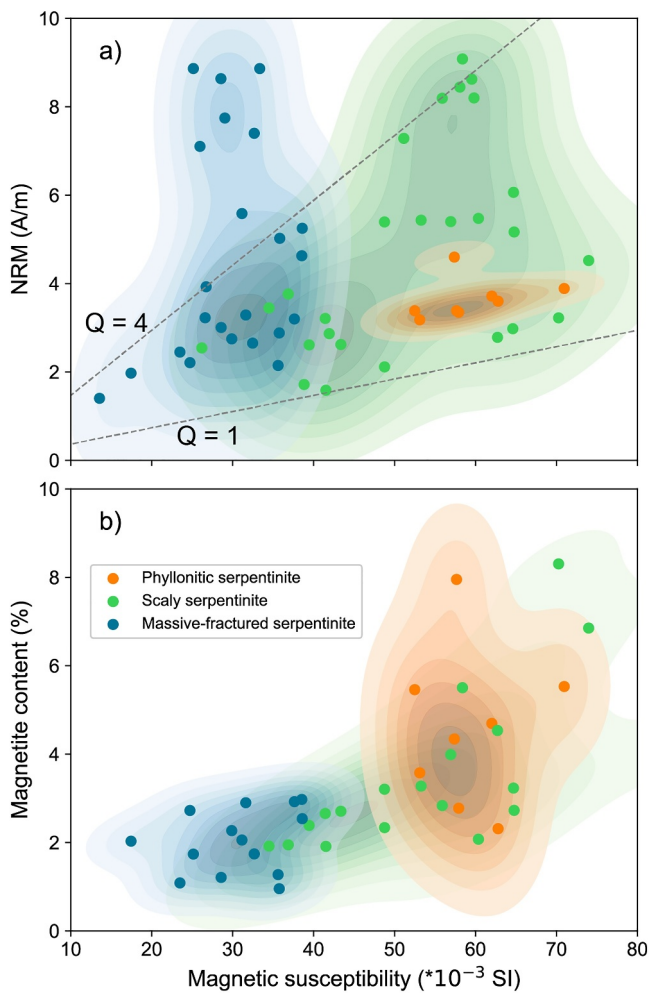


Figure 5. (a) Bulk magnetic susceptibility changes with the NRM intensity. Königsberg ratio (Q) is calculated for a field of 46,200 nT (current field in the Dhierona shear zone). (b) Magnetic susceptibility against magnetite volume contents determined by the saturation magnetization values. The darkness of background colors is encoded by the probability density of magnetic susceptibility, NRM intensity and magnetite contents.

Such deviations from ideal magnetite can reduce thermal stability, resulting in lower unblocking temperatures compared to the TRM-carrying magnetite (e.g., Schmidbauer & Keller, 2006).

The mean paleomagnetic direction for the massive-fractured serpentinite sites excluding M1 is $D = 309^\circ$, $I = 28^\circ$, $\alpha_{95} = 10^\circ$. The scaly and phyllonitic serpentinite sites excluding S5 have a mean direction of $D = 339^\circ$, $I = 29^\circ$, $\alpha_{95} = 8^\circ$. The single site from the gabbro intrusion shows a mean direction of $D = 313^\circ$, $I = 31^\circ$, $\alpha_{95} = 7^\circ$. The M1 and S5 localities exhibit paleomagnetic directions that differ from any of the serpentinite suite mean directions (Figure 6). These non-consistent directions indicate complex magnetization and deformation history within the transform zone.

5. Discussion

A sequence of serpentinite formations near the Dhierona shear zone ranges from less deformed massive-fractured serpentinites adjacent to the shear zone to highly deformed scaly and phyllonitic serpentinites within the shear zone (Figure 2). These serpentinites exhibit distinct microstructures, including undeformed mesh textures, deformed ribbon and fibrous structures. Analysis using SEM and Raman spectroscopy shows the replacement of lizardite by chrysotile as the serpentinite transitions from mesh to ribbon and fibrous structures (Figure 3). Rock magnetic results suggest that the scaly and phyllonitic serpentinites have coarser magnetic grain sizes (Figure 4), higher magnetic susceptibility and greater magnetite contents (Figure 5) compared to the massive-fractured serpentinite. Meanwhile, varying paleomagnetic directions are recorded in these differentially deformed serpentinites, pointing to a complex deformation and magnetization history associated with the oceanic transform zone (Figure 6).

5.1. Serpentine Replacement and Fe-Mg Exchange Within Deformed Serpentine

From massive serpentinite to scaly and phyllonitic serpentinites, lizardite is broken down into chrysotile through a dissolution-recrystallization process, which is evident in the oriented ribbon and fibrous microstructures (Figure 3). Then what about Fe behavior during the serpentine replacement of lizardite by chrysotile? Our EDX data show the total Fe content of lizardite mainly ranges from 5% to 7%, while in chrysotile, it is generally <4% (Figure 7a). Meanwhile, lizardite contains lower $MgO + Al_2O_3$ than chrysotile. Since the

Al_2O_3 content remains consistently low <1–2%, this suggests an exchange of Fe for Mg occurs during the replacement of lizardite by chrysotile. Previous studies have suggested similar Fe-Mg exchange behavior, such as a proposed equilibrium, $Fe_3Si_2O_5(OH)_4$ (Fe lizardite) + $3 Mg(OH)_2 = Mg_3Si_2O_5(OH)_4$ (Mg Chrysotile) + $3Fe(OH)_2$ by O'Hanley and Dyar (1998). Although this equilibrium assumes 100% Fe-Mg exchange between lizardite and chrysotile, the actual extent of the exchange varies depending on specific tectonic settings and would require detailed electron microprobe measurements, which is beyond the scope of this study. Importantly, the exchange of Fe for Mg implies that more Fe releases from serpentine minerals and might affect the magnetite formation in serpentinite.

5.2. Magnetite Formation Within Deformed Serpentine

The magnetite formation mechanism within deformed serpentinite is the basis for understanding the magnetic effects of serpentinite in tectonically active zones. Our magnetic results suggest a magnetite enhancement process is evident within the deformed serpentinite. This is indicated by the higher magnetic susceptibility values and magnetite contents observed as serpentinites change from the massive-fractured to the scaly and phyllonitic forms

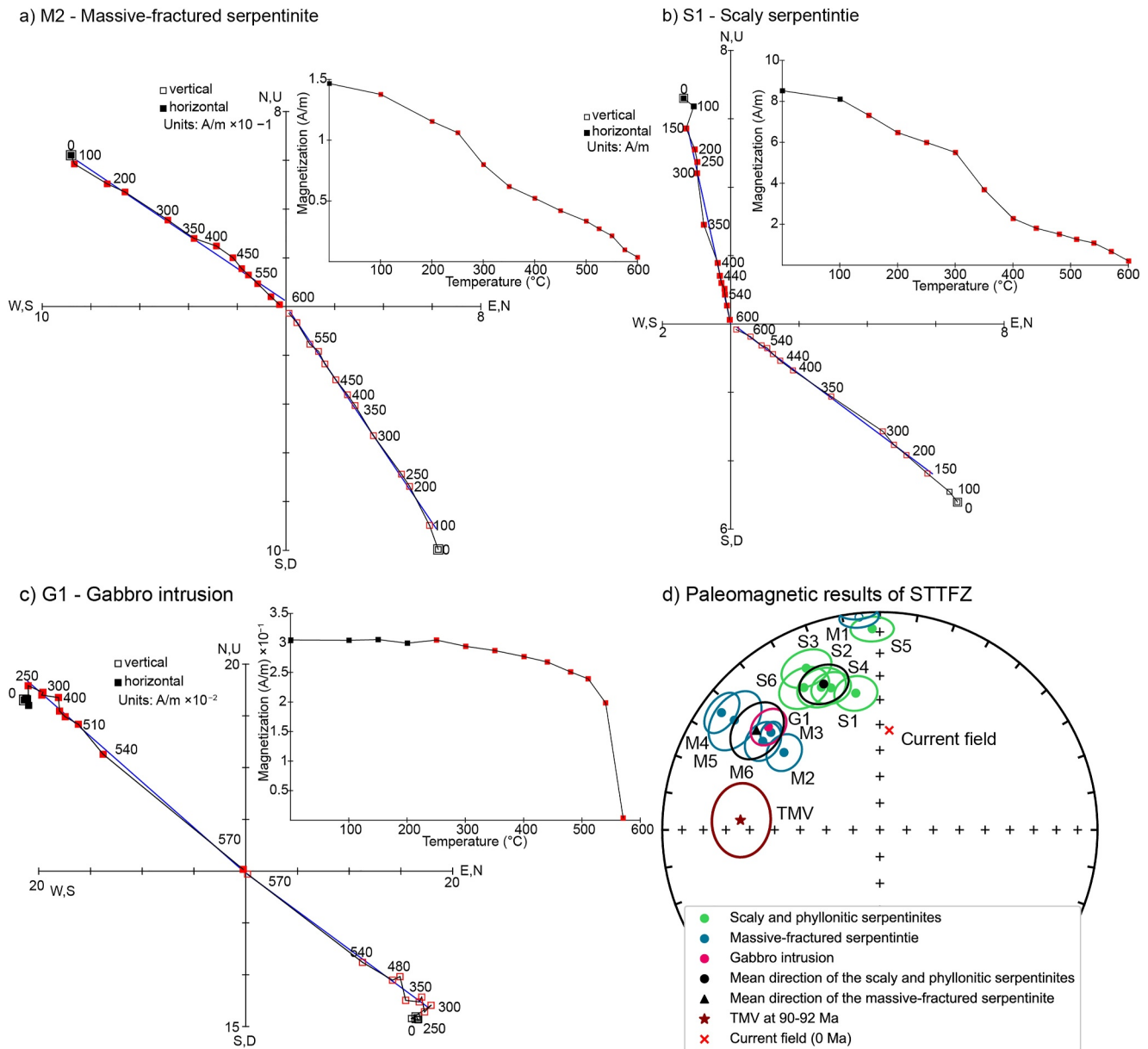


Figure 6. Representative orthogonal projection plots and demagnetization data for panel (a) massive-fractured serpentinite, (b) scaly phyllonitic serpentinite and (c) syn-transform gabbro intrusion. Red dots are chosen data points for PCA analysis. PCA fits are plotted as blue lines. (d) Equal-area plots show ChRM paleomagnetic directions for the gabbro intrusion, massive-fractured, scaly and phyllonitic serpentinites at both site and suite levels. The TMV at 90–92 Ma and the current field are also plotted.

(Figure 5). We suggest that this increase in magnetite content is linked to the recrystallization of serpentinite from lizardite to chrysotile because serpentinite minerals are the dominant iron repository apart from magnetite.

The potential Fe-Mg exchange revealed by our EDX data (Figure 7a) suggests that more iron can be released during the replacement of iron-rich lizardite by iron-poor chrysotile. We speculate that the released iron first appears as iron brucite ($Fe(OH)_2$) (e.g., Bach et al., 2006; Beard et al., 2009), which oxidizes to form magnetite (e.g., Frost & Beard, 2007; Toft et al., 1990). If this hypothesis holds, there should be a strong correlation between the contents of lizardite, chrysotile and magnetite in the serpentinite. To explore this correlation, we examined 10 SEM images from different specimens, including three from massive-fractured serpentinite, four from scaly serpentinite and three from phyllonitic serpentinite. In these images, the different iron contents allow us to distinguish between the iron-rich lizardite, iron-poor chrysotile and magnetite: lizardite is dark gray, chrysotile

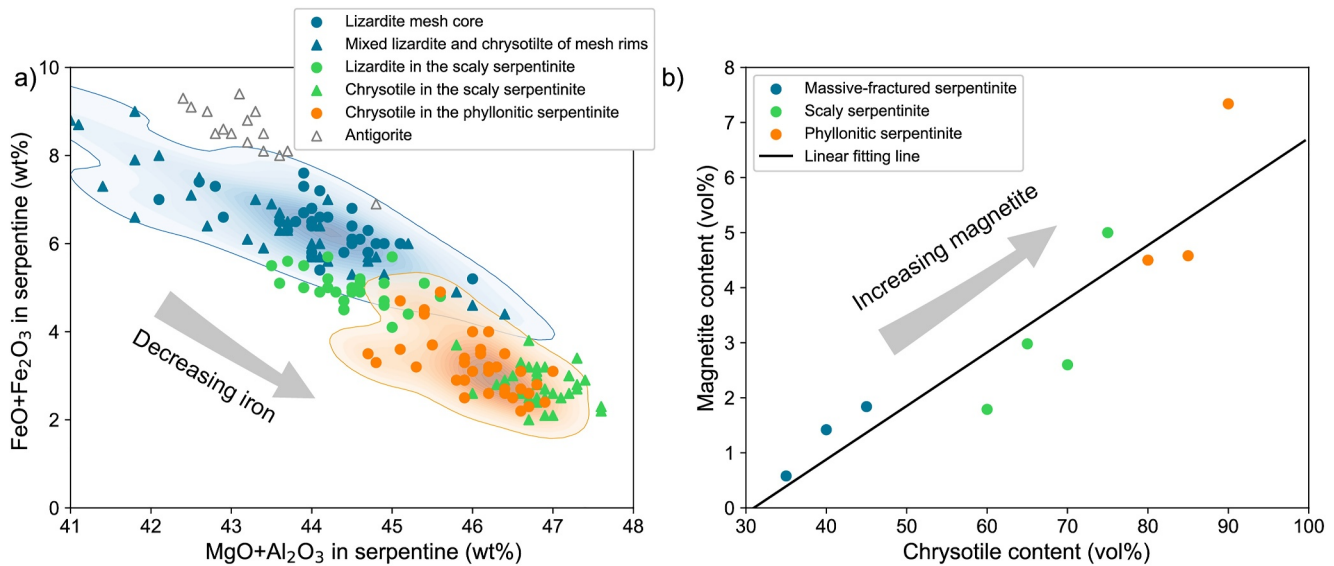


Figure 7. (a) The EDX analysis results. Oxide weight percent of total iron ($FeO + Fe_2O_3$) and metal cations without unpaired electrons ($MgO + Al_2O_3$) in serpentine minerals of the massive-fractured, scaly and phyllonitic serpentinites. Background colors are encoded by the probability density of serpentine iron content in massive-fractured and phyllonitic serpentinites. (b) The SEM image analysis results. Magnetite volume content increases linearly with chrysotile content in the massive-fractured, scaly and phyllonitic serpentinites.

appears as the darkest area and magnetite is the brightest mineral (Figure 3). The volume contents of lizardite, chrysotile and magnetite were estimated based on their respective area proportions in the SEM images. Figure 7b shows the SEM analysis results, indicating a linear increase of magnetite with chrysotile content in the massive-fractured serpentinite to scaly and phyllonitic serpentinites. This linear relationship supports our hypothesis that the formation of iron-poor chrysotile from iron-rich lizardite releases iron, which then contributes to the formation of magnetite. As a result, scaly and phyllonitic serpentinites exhibit higher magnetite concentration and magnetic susceptibility values, as shown in Figure 5b.

Apart from the variations of magnetite concentration, coarser magnetite grains are found in the highly deformed serpentinite than the less deformed one (Figure 4). Bigger magnetite grain sizes explain that despite higher magnetite content and bulk magnetic susceptibility, the scaly and phyllonitic serpentinites do not exhibit significantly higher NRM values compared to the massive-fractured serpentinites (Figure 5a). The coarser magnetite grains are likely due to high water/rock ratios in the shear zone with the development of macro-micro fractures, faults and S-C structures (Figure 2). The enhanced fluid activity is also consistent with the presence of dominant chrysotile in the deformed serpentinite because chrysotile is fluid-favored (Evans, 2004).

Our magnetite formation mechanism relies on the Fe-Mg exchange during the replacement of lizardite and chrysotile, emphasizing the enhanced hydrothermal fluid activity during the increasing deformation of serpentinite. This mechanism is consistent with results from existing studies of undeformed serpentinitized peridotite. For example, Evans (2008) found Fe-Mg exchange in chrysotile veins during the pore fluid attending serpentinization of olivine and orthopyroxene. Frost et al. (2013) reported iron-rich lizardite veins and iron-poor chrysotile veins in serpentinitized dunite from New Caledonia. The chrysotile veins are larger, later and contain more magnetite than the lizardite veins, implying magnetite formation with increasing fluid flux. Maffione et al. (2014) suggested that large MD magnetite grains were hosted by large serpentine veins due to high fluid flux.

5.3. Serpentinization, Magma Intrusions, Deformation and Remagnetization

Previously, we discussed serpentine replacement, chemical alterations and magnetite formation from massive-fractured to scaly and phyllonitic serpentinites. However, it is still not clear what kind of geological system has caused these mineral and chemical processes. For example, how did serpentinization occur, and what role did shear zone deformation play in this process?

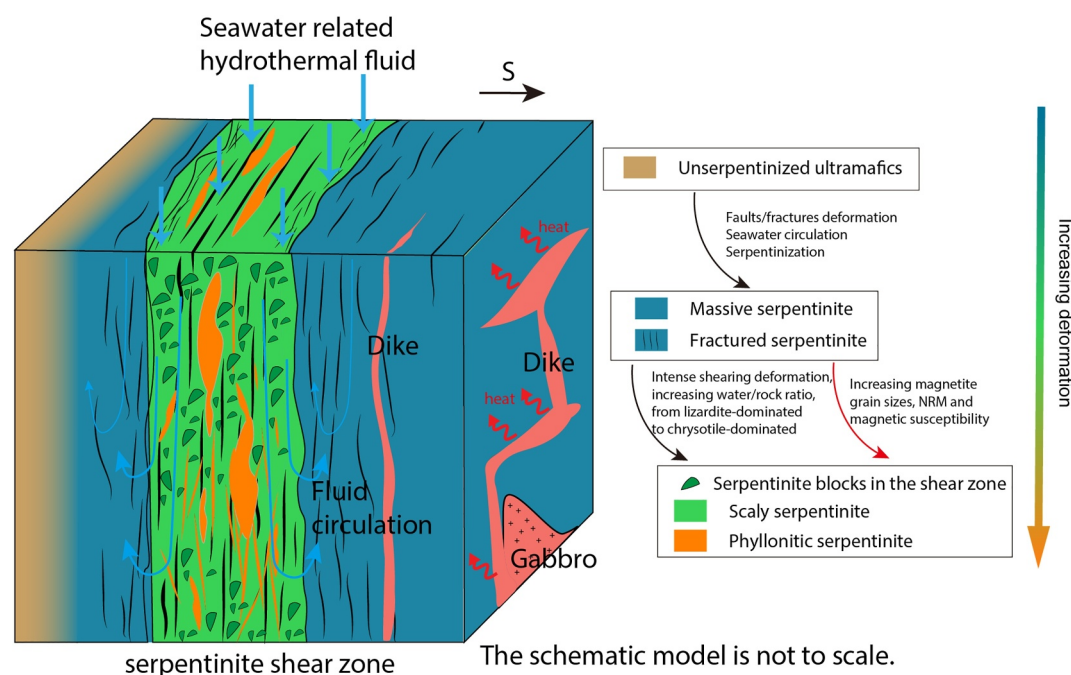


Figure 8. Schematic model illustrating the relationship between shearing deformation, seawater circulation, magma heat, serpentinization and variably deformed serpentinites (modified after Martin et al., 2023).

We suggest the serpentinized mantle lithosphere of the STTFZ was located below the seafloor, as there is no evidence of serpentinite exposure on the seafloor (Cox et al., 2021; Gass et al., 1994) (Figure 8). The presence of specific serpentine minerals observed in this study (Figure 3) constrains the temperature of serpentinization and deformation. Lizardite is the dominant mineral in the massive-fractured serpentinite, while chrysotile is prevalent in the scaly and phyllonitic serpentinites (Figure 3). We find minor amounts of antigorite in the phyllonitic serpentinite; Cox et al. (2021) reported antigorite in the massive serpentinite of this shear zone. The presence of lizardite, chrysotile and antigorite suggests that serpentinization occurs at a temperature range where these serpentine minerals remain stable. The lizardite and chrysotile are stable at $T < 400^{\circ}\text{C}$, while the antigorite is stable above 300°C (Evans, 2004; Schwartz et al., 2013). The predominance of lizardite and chrysotile without antigorite in most serpentinites indicates that temperatures are generally below 300°C . The formation of magnetite during serpentinization also provides a lower temperature limit, as iron is more readily incorporated into magnetite than serpentine at $T > 200^{\circ}\text{C}$ (Bonnemains et al., 2016; Klein et al., 2014; Rouméjon et al., 2018). Therefore, serpentinization in the STTFZ is generally constrained to a temperature range of $200\text{--}300^{\circ}\text{C}$, while localized areas reach up to $300\text{--}400^{\circ}\text{C}$. This range is comparable to the serpentinization temperature of the present-day Rainbow hydrothermal vent field (e.g., Evans et al., 2024). The magma intrusions, like gabbro and dike observed near the Dhierona serpentinite shear zone, have been suggested to provide heat to the hydrothermal alteration (e.g., Martin et al., 2023) (Figure 8). Similar magma-serpentinization settings have been reported along the slow-ultraslow mid-oceanic ridges, such as the mid-Atlantic ridge (e.g., Searle et al., 2019; Smith et al., 2008).

Apart from the heat from magma, faults and fractures within the transform fault zone extended into deep ultramafic rocks, acting as conduits for seawater to penetrate the crust and interact with ultramafic rocks (Figure 8) (Cox et al., 2021; Martin et al., 2023). Serpentinization occurred, releasing iron from olivine and pyroxene and forming finer-grain magnetite in the massive-fractured serpentinite. Due to the much weaker mechanical properties of serpentinite compared to fresh peridotite (Kuna et al., 2019), deformation was localized in serpentinized rocks, forming a serpentinite shear zone. Within the shear zone, enhanced fluid activities were expected, leading to the replacement of lizardite by fluid-favored chrysotile, which released iron and formed coarser-grained magnetite in scaly and phyllonitic serpentinites. These two magnetite formation mechanisms imply different chemical remagnetization pathways in serpentinites with varying degrees of deformation, occurring simultaneously or in close succession when magma intrusions (gabbros/dikes) and the transform faulting were active (Figure 8).

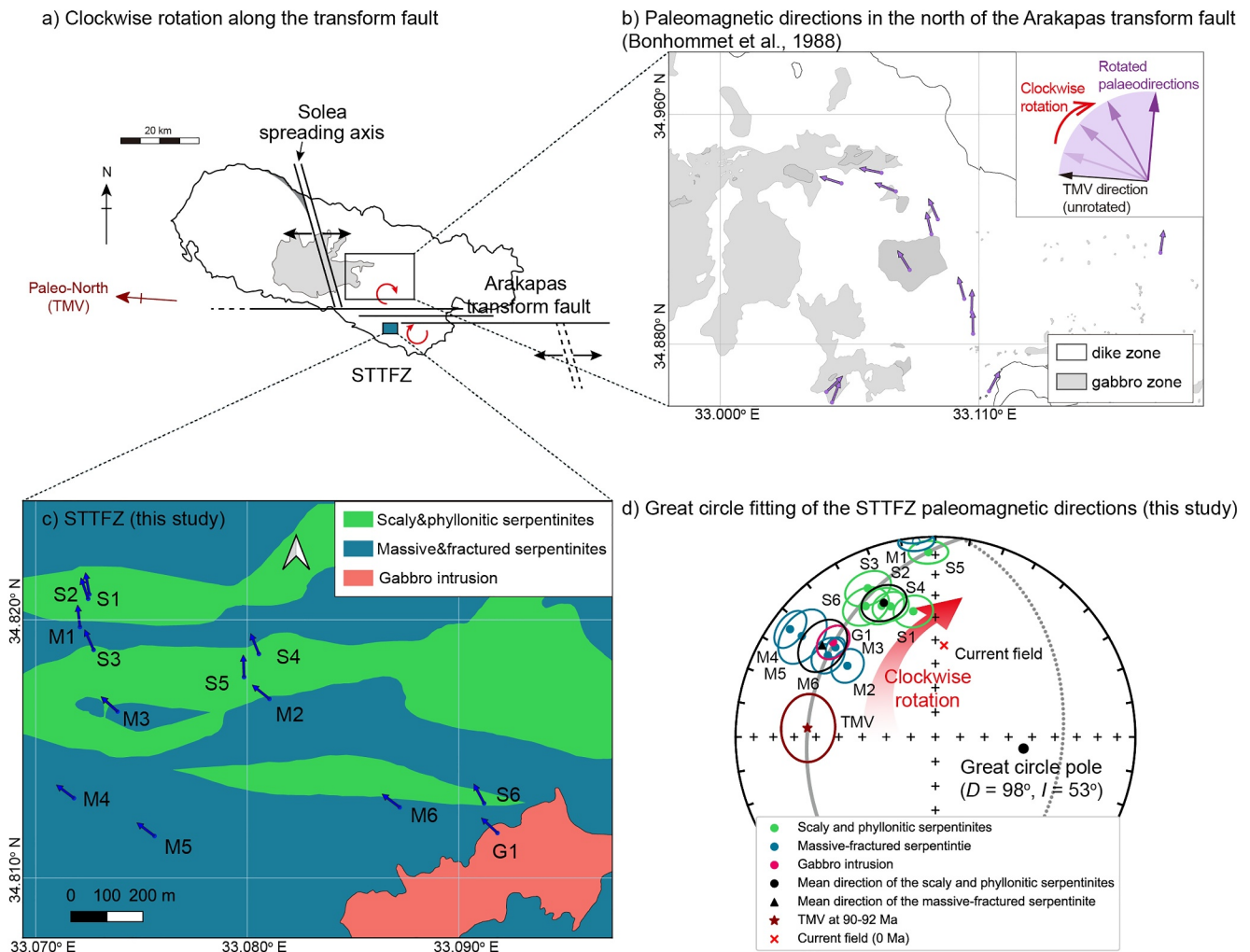


Figure 9. (a) The ridge-transform model illustrates clockwise block rotations in the inner corner and transform fault zone. (b) Purple arrows, encoded by the paleomagnetic declinations from dikes, show the clockwise block rotation along the transform fault (Bonhommet et al., 1988). (c) A geological map based on our field descriptions and those of Cox et al. (2021), overlain with blue arrows indicating the paleomagnetic declinations. Clockwise rotations of up to $\sim 90^\circ$ were found. (d) Great circle fitting of the TMV, serpentinite and gabbro paleomagnetic directions of this study, shows a common rotation axis of $D = 98^\circ$, $I = 53^\circ$.

5.4. Syn-Transform Clockwise Rotation After Chemical Remagnetization

Based on the discussion above, the massive-fractured, scaly and phyllonitic serpentinites should acquire the same CRM direction in the TMV field, similar to the gabbro TRM direction. However, our paleomagnetic results from variably deformed serpentinites and the gabbro intrusion show significant deviations from the TMV direction (Figure 6d). This suggests that these differentially deformed serpentinites and gabbro have undergone varying degrees of tectonic rotation after acquiring their magnetization.

Inner-block rotations within the ophiolite have been proposed to accommodate the transform fault-related shearing (Figure 9a). For example, paleomagnetic data from dikes along the northern boundary of the Arakapas transform fault suggest a $\sim 90^\circ$ clockwise rotation (Figure 9b) (Bonhommet et al., 1988). In this study, CRM directions recorded in the differentially deformed serpentinites provide evidence of the rotation mechanism within the STTFZ (Figure 9c). Our analysis shows that the directions of the TMV, the syn-transform gabbro intrusion, and the massive-fractured, scaly and phyllonitic serpentinites align along a great circle with a pole at $D = 98^\circ$, $I = 53^\circ$ (Figure 9d). This alignment indicates significant clockwise block rotations. The smallest rotation angle ($\sim 30^\circ$) is observed between the TMV and the massive-fractured serpentinite and gabbro intrusion. The largest rotation angle reaches up to 90° , noted between the TMV and the serpentinite at the M1 and S5 localities.

The rotation angle for most scaly and phyllonitic serpentinites is $\sim 60^\circ$, larger than the massive-fractured serpentinite.

A simple interpretation of these paleomagnetic directions is that the variably deformed serpentinites and gabbro recorded clockwise block rotations associated with the dextral Arakapas transform fault zone (Figure 9c). The closer to the transform fault, the nearer to the rotation center, and the higher the rotation angles, similar to the rotation trend observed in dike directions (Figure 9b) (Bonhommet et al., 1988). These clockwise rotations likely occurred at a low temperature during the final stage of ophiolite formation (Figure 9), when the dextral transform shearing continued after the decrease or cessation of magma supply (Hurst et al., 1994). Therefore, this clockwise rotation happens after the acquisition of chemical magnetizations in serpentinite when magma was still active (Sections 5.3) (Figure 8).

In summary, our paleomagnetic directions suggest up to 90° of clockwise rotation associated with transform shearing. When combined with the dike data from Bonhommet et al. (1988), we provide robust evidence for dextral shearing of the STTFZ (Figure 9). Compared to Morris et al. (1990), our study suggests that dextral transform shearing occurred in the deep mantle, rather than being constrained to the shallow sediments and lavas currently situated along the boundary of the STTFZ.

6. Conclusions

Our study systematically investigates the transformation of serpentine minerals, magnetic properties, magnetite formation mechanisms and remagnetization recorded in serpentinite under increasing deformation. A geological model involving deformation, seawater circulation, magma-driven heating, hydrothermal alteration, and chemical remagnetization has been proposed for an oceanic transform fault setting. As serpentinite deformation increases from massive-fractured serpentinite to scaly and phyllonitic serpentinites, the predominant serpentine minerals change from iron-rich lizardite to iron-poor chrysotile (Figure 3). The replacement of lizardite by chrysotile releases iron and facilitates the formation of magnetite within the highly deformed serpentinite (Figure 7). Meanwhile, compared to the less deformed serpentinite, coarser PSD magnetite grains are found in the deformed serpentinite due to enhanced fluid activity (Figure 8). These magnetite grains carry remagnetization, which can be used to reconstruct complex rotation history within tectonically active zones. For example, paleomagnetic directions of the differentially deformed serpentinites within the STTFZ suggest a clockwise tectonic rotation of up to $\sim 90^\circ$ (Figure 9), serving as robust evidence for the dextral slip of the transform fault.

Data Availability Statement

The measured data relevant to this paper are available in Qi et al. (2024).

References

- Allerton, S., & Vine, F. J. (1991). Spreading evolution of the Troodos ophiolite, Cyprus. *Geology*, *19*(6), 637–640. [https://doi.org/10.1130/0091-7613\(1991\)019<0637:Seotto>2.3.Co;2](https://doi.org/10.1130/0091-7613(1991)019<0637:Seotto>2.3.Co;2)
- Bach, W., Paulick, H., Garrido, C. J., Ildefonse, B., Meurer, W. P., & Humphris, S. E. (2006). Unraveling the sequence of serpentinization reactions: Petrography, mineral chemistry, and petrophysics of serpentinites from MAR 15°N (ODP Leg 209, site 1274). *Geophysical Research Letters*, *33*(13), L13306. <https://doi.org/10.1029/2006GL025681>
- Beard, J. S., Frost, B. R., Fryer, P., McCaig, A., Searle, R., Ildefonse, B., et al. (2009). Onset and progression of serpentinization and magnetite formation in olivine-rich troctolite from IODP Hole U1309D. *Journal of Petrology*, *50*(3), 387–403. <https://doi.org/10.1093/ptrology/egp004>
- Bonhommet, N., Roperch, P., & Calza, F. (1988). Paleomagnetic arguments for block rotations along the Arakapas fault (Cyprus). *Geology*, *16*(5), 422–425. [https://doi.org/10.1130/0091-7613\(1988\)016<0422:Pafbra>2.3.Co;2](https://doi.org/10.1130/0091-7613(1988)016<0422:Pafbra>2.3.Co;2)
- Bonnemains, D., Carlut, J., Escartín, J., Mével, C., Andreani, M., & Debret, B. (2016). Magnetic signatures of serpentinization at ophiolite complexes. *Geochemistry, Geophysics, Geosystems*, *17*(8), 2969–2986. <https://doi.org/10.1002/2016GC006321>
- Chen, Y., Niu, Y., Shen, F., Gao, Y., & Wang, X. (2020). New U-Pb zircon age and petrogenesis of the plagiogranite, Troodos ophiolite, Cyprus. *Lithos*, *362*–363, 105472. <https://doi.org/10.1016/j.lithos.2020.105472>
- Clube, T. M. M., Creer, K., & Robertson, A. (1985). Palaeorotation of the Troodos microplate, Cyprus. *Nature*, *317*(6037), 522–525. <https://doi.org/10.1038/317522a0>
- Cox, S., Fagereng, Å., & MacLeod, C. J. (2021). Shear zone development in serpentinized mantle: Implications for the strength of oceanic transform faults. *Journal of Geophysical Research: Solid Earth*, *126*(5), e2020JB020763. <https://doi.org/10.1029/2020JB020763>
- Davy, R., Collier, J., Henstock, T., Consortium, V., Rietbrock, A., Goes, S., et al. (2020). Wide-angle seismic imaging of two modes of crustal accretion in mature Atlantic Ocean crust. *Journal of Geophysical Research: Solid Earth*, *125*(6), e2019JB019100. <https://doi.org/10.1029/2019JB019100>
- Day, R., Fuller, M., & Schmidt, V. (1977). Hysteresis properties of titanomagnetites: Grain-size and compositional dependence. *Physics of the Earth and Planetary Interiors*, *13*(4), 260–267. [https://doi.org/10.1016/0031-9201\(77\)90108-X](https://doi.org/10.1016/0031-9201(77)90108-X)
- Dunlop, D. J., & Özdemir, Ö. (2001). *Rock magnetism: Fundamentals and frontiers*. Cambridge University Press.

Acknowledgments

L.Q. thanks the Gray-Milne travel fund from the British Geophysical Association, which partially supported the fieldwork for this study. A.R.M. acknowledges funding from UKRI Grant NE/V001388/1. The authors thank the Editor Mark Dekkers, the Associate Editor and two anonymous reviewers for their professional review work and valuable suggestions. The authors also extend their gratitude to the Cyprus Geological Surveying Department for their generous assistance, particularly to Director Christodoulos Hadjigeorgiou, Vasilis Symeou, and Nik Papadimitriou. Thanks are also due to Raul Adriaensen for his help with paleomagnetic sampling. This work utilized expertise and prototyping equipment at the Imperial Advanced Hackspace.

- Dyment, J., & Arkani-Hamed, J. (1995). Spreading-rate-dependent magnetization of the oceanic lithosphere inferred from the anomalous skewness of marine magnetic anomalies. *Geophysical Journal International*, *121*(3), 789–804. <https://doi.org/10.1111/j.1365-246X.1995.tb06439.x>
- Evans, B. W. (2004). The serpentinite multisystem revisited: Chrysotile is metastable. *International Geology Review*, *46*(6), 479–506. <https://doi.org/10.2747/0020-6814.46.6.479>
- Evans, B. W. (2008). Control of the products of serpentinization by the Fe²⁺+Mg–1 exchange potential of olivine and orthopyroxene. *Journal of Petrology*, *49*(10), 1873–1887. <https://doi.org/10.1093/ptrology/egn050>
- Evans, B. W., Hattori, K., & Baronnet, A. (2013). Serpentinite: What, why, where? *Elements*, *9*(2), 99–106. <https://doi.org/10.2113/gselements.9.2.99>
- Evans, G. N., Awolayo, A. N., Tutolo, B. M., & Seyfried, W. E. (2024). Geochemical constraints on reaction temperature and pressure and heat- and mass-transfer efficiency at Rainbow Hydrothermal Field. *Earth and Planetary Science Letters*, *648*, 119063. <https://doi.org/10.1016/j.epsl.2024.119063>
- Fisher, R. A. (1953). Dispersion on a sphere. *Proceedings of the Royal Society of London. Series A. Mathematical and Physical Sciences*, *217*(1130), 295–305. <https://doi.org/10.1098/rspa.1953.0064>
- Frost, B. R., & Beard, J. S. (2007). On silica activity and serpentinization. *Journal of Petrology*, *48*(7), 1351–1368. <https://doi.org/10.1093/ptrology/egm021>
- Frost, B. R., Evans, K. A., Swapp, S. M., Beard, J. S., & Mothersole, F. E. (2013). The process of serpentinization in dunite from New Caledonia. *Lithos*, *178*, 24–39. <https://doi.org/10.1016/j.lithos.2013.02.002>
- Gass, I. G., MacLeod, C. J., Murton, B. J., Panayiotou, A., Simonian, K. O., & Xenophontos, C. (1994). *The geological evolution of the Southern Troodos transform fault zone* (Vol. 9). Geological Survey Department.
- Guillot, S., Schwartz, S., Reynard, B., Agard, P., & Prigent, C. (2015). Tectonic significance of serpentinites. *Tectonophysics*, *646*, 1–19. <https://doi.org/10.1016/j.tecto.2015.01.020>
- Harrison, R. J., & Feinberg, J. M. (2008). FORCinel: An improved algorithm for calculating first-order reversal curve distributions using locally weighted regression smoothing. *Geochemistry, Geophysics, Geosystems*, *9*(5), Q05016. <https://doi.org/10.1029/2008GC001987>
- Hodel, F., Macouin, M., Trindade, R. I. F., Araujo, J. F. D. F., Respaud, M., Meunier, J. F., et al. (2020). Magnetic properties of ferritchromite and magnetite and monitoring of Cr-spinels alteration in ultramafic and mafic rocks. *Geochemistry, Geophysics, Geosystems*, *21*(11), e2020GC009227. <https://doi.org/10.1029/2020GC009227>
- Hurst, S. D., Moores, E. M., & Varga, R. J. (1994). Structural and geophysical expression of the Solea graben, Troodos Ophiolite, Cyprus. *Tectonics*, *13*(1), 139–156. <https://doi.org/10.1029/93TC02066>
- Kirschvink, J. L. (1980). The least-squares line and plane and the analysis of palaeomagnetic data. *Geophysical Journal International*, *62*(3), 699–718. <https://doi.org/10.1111/j.1365-246X.1980.tb02601.x>
- Klein, F., Bach, W., Humphris, S. E., Kahl, W.-A., Jöns, N., Moskowit, B., & Berquó, T. S. (2014). Magnetite in seafloor serpentinite—Some like it hot. *Geology*, *42*(2), 135–138. <https://doi.org/10.1130/G35068.1>
- Klein, F., Goldsby, D. L., Lin, J., & Andreani, M. (2022). Carbonation of serpentinite in creeping faults of California. *Geophysical Research Letters*, *49*(15), e2022GL099185. <https://doi.org/10.1029/2022GL099185>
- Kuna, V. M., Nábělek, J. L., & Braunmiller, J. (2019). Mode of slip and crust–mantle interaction at oceanic transform faults. *Nature Geoscience*, *12*(2), 138–142. <https://doi.org/10.1038/s41561-018-0287-1>
- Lurcock, P. C., & Wilson, G. S. (2012). PuffinPlot: A versatile, user-friendly program for paleomagnetic analysis. *Geochemistry, Geophysics, Geosystems*, *13*(6). <https://doi.org/10.1029/2012gc004098>
- MacLeod, C., & Murton, B. (1993). Structure and tectonic evolution of the Southern Troodos transform fault zone, Cyprus. *Geological Society, London, Special Publications*, *76*(1), 141–176. <https://doi.org/10.1144/GSL.SP.1993.076.01.0>
- MacLeod, C. J., Allerton, S., Gass, I., & Xenophontos, C. (1990). Structure of a fossil ridge–transform intersection in the Troodos ophiolite. *Nature*, *348*(6303), 717–720. <https://doi.org/10.1038/348717a0>
- MacLeod, C. J., & Murton, B. J. (1995). On the sense of slip of the Southern Troodos transform fault zone, Cyprus. *Geology*, *23*(3), 257–260. [https://doi.org/10.1130/0091-7613\(1995\)023<0257:Otsoso>2.3.Co;2](https://doi.org/10.1130/0091-7613(1995)023<0257:Otsoso>2.3.Co;2)
- Maffione, M., Morris, A., Plümper, O., & Van Hinsbergen, D. J. (2014). Magnetic properties of variably serpentinized peridotites and their implication for the evolution of oceanic core complexes. *Geochemistry, Geophysics, Geosystems*, *15*(4), 923–944. <https://doi.org/10.1002/2013GC004993>
- Martin, A. J., MacLeod, C. J., McFall, K. A., McDonald, I., Jamieson, J. W., & Cox, S. (2023). Ultramafic-hosted Ni-Cu-Co-(As) mineralization from an ancient oceanic transform fault zone in the Troodos ophiolite, Cyprus: An analogue for ultramafic sea-floor massive sulfide mineralization? *Economic Geology*, *118*(5), 1125–1147. <https://doi.org/10.5382/econgeo.4996>
- Mével, C. (2003). Serpentinization of abyssal peridotites at mid-ocean ridges. *Comptes Rendus Geoscience*, *335*(10–11), 825–852. <https://doi.org/10.1016/j.crte.2003.08.006>
- Miller, D. J., & Christensen, N. I. (1997). Seismic velocities of lower crustal and upper mantle rocks from the slow-spreading Mid-Atlantic Ridge, south of the Kane Transform Zone (MARK). *Proceedings of the Ocean Drilling Program*. <https://doi.org/10.2973/odp.proc.sr.153.043.1997>
- Moore, D. E., & Rymer, M. J. (2007). Talc-bearing serpentinite and the creeping section of the San Andreas Fault. *Nature*, *448*(7155), 795–797. <https://doi.org/10.1038/nature06064>
- Moores, E., & Vine, F. J. (1971). The Troodos massif, Cyprus and other ophiolites as oceanic crust: Evaluation and implications. *Philosophical Transactions of the Royal Society of London - Series A: Mathematical and Physical Sciences*, *268*(1192), 443–467. <https://doi.org/10.1098/rsta.1971.0006>
- Morris, A. (1996). A review of palaeomagnetic research in the Troodos ophiolite. *Geological Society, London, Special Publications*, *105*(1), 311–324. <https://doi.org/10.1144/GSL.SP.1996.105.01.2>
- Morris, A., Creer, K., & Robertson, A. (1990). Palaeomagnetic evidence for clockwise rotations related to dextral shear along the southern Troodos transform fault, Cyprus. *Earth and Planetary Science Letters*, *99*(3), 250–262. [https://doi.org/10.1016/0012-821X\(90\)90114-D](https://doi.org/10.1016/0012-821X(90)90114-D)
- Morris, A., & Maffione, M. (2016). Is the Troodos ophiolite (Cyprus) a complete, transform fault–bounded Neotethyan ridge segment? *Geology*, *44*(3), 199–202. <https://doi.org/10.1130/g37529.1>
- Mukasa, S. B., & Ludden, J. N. (1987). Uranium-lead isotopic ages of plagiogranites from the Troodos ophiolite, Cyprus, and their tectonic significance. *Geology*, *15*(9), 825–828. [https://doi.org/10.1130/0091-7613\(1987\)15<825:Uiaopf>2.0.Co;2](https://doi.org/10.1130/0091-7613(1987)15<825:Uiaopf>2.0.Co;2)
- Murton, B. (1986). Anomalous oceanic lithosphere formed in a leaky transform fault: Evidence from the western limassol forest complex, Cyprus. *Journal of the Geological Society*, *143*(5), 845–854. <https://doi.org/10.1144/gsjgs.143.5.0845>
- Muxworthy, A. R., Turney, J. N., Qi, L., Baker, E. B., Perkins, J. R., & Abdulkarim, M. A. (2023). Interpreting high-temperature magnetic susceptibility data of natural systems. *Frontiers in Earth Science*, *11*, 1171200. <https://doi.org/10.3389/feart.2023.1171200>

- Nagy, L., Moreno, R., Muxworthy, A. R., Williams, W., Paterson, G. A., Tauxe, L., & Valdez-Grijalva, M. A. (2024). Micromagnetic determination of the FORC response of paleomagnetically significant magnetite assemblages. *Geochemistry, Geophysics, Geosystems*, 25(7), e2024GC011465. <https://doi.org/10.1029/2024GC011465>
- Nuriel, P., Katzir, Y., Abelson, M., Valley, J. W., Matthews, A., Spicuzza, M. J., & Ayalon, A. (2009). Fault-related oceanic serpentinization in the Troodos ophiolite, Cyprus: Implications for a fossil oceanic core complex. *Earth and Planetary Science Letters*, 282(1–4), 34–46. <https://doi.org/10.1016/j.epsl.2009.02.029>
- O'Hanley, D. S., & Dyar, M. D. (1998). The composition of chrysotile and its relationship with lizardite. *The Canadian Mineralogist*, 36(3), 727–739.
- Oufi, O., Cannat, M., & Horen, H. (2002). Magnetic properties of variably serpentinized abyssal peridotites. *Journal of Geophysical Research*, 107(B5). <https://doi.org/10.1029/2001JB000549>
- Pauthenet, R., & Bochirol, L. (1951). Aimantation spontanée des ferrites. *Journal de Physique et le Radium*, 12(3), 249–251. <https://doi.org/10.1051/jphysrad:01951001203024900>
- Pearce, J. A., Lippard, S., & Roberts, S. (1984). Characteristics and tectonic significance of supra-subduction zone ophiolites. *Geological Society, London, Special Publications*, 16(1), 77–94. <https://doi.org/10.1144/GSL.SP.1984.016.01.06>
- Qi, L., Allerton, S., Muxworthy, A. R., Zhang, Y., & Gergov, H. (2024). Magnetic properties and chemical compositions of differentially deformed serpentinites in an ancient transform fault zone of the Troodos ophiolite [Dataset]. *Zenodo*. <https://doi.org/10.5281/zenodo.14179301>
- Roberts, A. P., Heslop, D., Zhao, X., & Pike, C. R. (2014). Understanding fine magnetic particle systems through use of first-order reversal curve diagrams. *Reviews of Geophysics*, 52(4), 557–602. <https://doi.org/10.1002/2014RG000462>
- Roberts, A. P., Pike, C. R., & Verosub, K. L. (2000). First-order reversal curve diagrams: A new tool for characterizing the magnetic properties of natural samples. *Journal of Geophysical Research*, 105(B12), 28461–28475. <https://doi.org/10.1029/2000JB900326>
- Rooney, J. S., Tarling, M. S., Smith, S. A. F., & Gordon, K. C. (2018). Submicron Raman spectroscopy mapping of serpentinite fault rocks. *Journal of Raman Spectroscopy*, 49(2), 279–286. <https://doi.org/10.1002/jrs.5277>
- Roumèjon, S., Williams, M. J., & Früh-Green, G. L. (2018). In-situ oxygen isotope analyses in serpentine minerals: Constraints on serpentinization during tectonic exhumation at slow- and ultraslow-spreading ridges. *Lithos*, 323, 156–173. <https://doi.org/10.1016/j.lithos.2018.09.021>
- Schiffman, P., Smith, B. M., Varga, R. J., & Moores, E. M. (1987). Geometry, conditions and timing of off-axis hydrothermal metamorphism and ore-deposition in the Solea graben. *Nature*, 325(6103), 423–425. <https://doi.org/10.1038/325423a0>
- Schmidbauer, E., & Keller, M. (2006). Magnetic hysteresis properties, Mössbauer spectra and structural data of spherical 250nm particles of solid solutions Fe₃O₄–γ-Fe₂O₃. *Journal of Magnetism and Magnetic Materials*, 297(2), 107–117. <https://doi.org/10.1016/j.jmmm.2005.02.063>
- Schwartz, S., Guillot, S., Reynard, B., Lafay, R., Debret, B., Nicolle, C., et al. (2013). Pressure–temperature estimates of the lizardite/antigorite transition in high pressure serpentinites. *Lithos*, 178, 197–210. <https://doi.org/10.1016/j.lithos.2012.11.023>
- Searle, R. C., MacLeod, C. J., Peirce, C., & Reston, T. J. (2019). The mid-Atlantic ridge near 13°20'N: High-resolution magnetic and bathymetry imaging. *Geochemistry, Geophysics, Geosystems*, 20(1), 295–313. <https://doi.org/10.1029/2018GC007940>
- Simonian, K. O., & Gass, I. G. (1978). Arakapas fault belt, Cyprus: A fossil transform fault. *GSA Bulletin*, 89(8), 1220–1230. [https://doi.org/10.1130/0016-7606\(1978\)89<1220:Afbcaf>2.0.CO;2](https://doi.org/10.1130/0016-7606(1978)89<1220:Afbcaf>2.0.CO;2)
- Smith, D. K., Escartín, J., Schouten, H., & Cann, J. R. (2008). Fault rotation and core complex formation: Significant processes in seafloor formation at slow-spreading mid-ocean ridges (Mid-Atlantic Ridge, 13°–15°N). *Geochemistry, Geophysics, Geosystems*, 9(3), Q03003. <https://doi.org/10.1029/2007gc001699>
- Szitkar, F., Tivey, M. A., Kelley, D. S., Karson, J. A., Früh-Green, G. L., & Denny, A. R. (2017). Magnetic exploration of a low-temperature ultramafic-hosted hydrothermal site (Lost City, 30°N, MAR). *Earth and Planetary Science Letters*, 461, 40–45. <https://doi.org/10.1016/j.epsl.2016.12.033>
- Tarling, M. S., Rooney, J. S., Viti, C., Smith, S. A. F., & Gordon, K. C. (2018). Distinguishing the Raman spectrum of polygonal serpentine. *Journal of Raman Spectroscopy*, 49(12), 1978–1984. <https://doi.org/10.1002/jrs.5475>
- Toft, P. B., Arkani-Hamed, J., & Haggerty, S. E. (1990). The effects of serpentinization on density and magnetic susceptibility: A petrophysical model. *Physics of the Earth and Planetary Interiors*, 65(1–2), 137–157. [https://doi.org/10.1016/0031-9201\(90\)90082-9](https://doi.org/10.1016/0031-9201(90)90082-9)
- Varga, R. J., & Moores, E. M. (1985). Spreading structure of the Troodos ophiolite, Cyprus. *Geology*, 13(12), 846–850. [https://doi.org/10.1130/0091-7613\(1985\)13<846:SSOTTO>2.0.CO;2](https://doi.org/10.1130/0091-7613(1985)13<846:SSOTTO>2.0.CO;2)
- Yu, Y., & Tikoff, B. (2020). Magnetic Cr-rich spinel in serpentinized ultramafic complexes. *Journal of Geophysical Research: Solid Earth*, 125(11), e2020JB020443. <https://doi.org/10.1029/2020JB020443>
- Yuan, X., & Mayanovic, R. A. (2017). An empirical study on Raman peak fitting and its application to Raman quantitative research. *Applied Spectroscopy*, 71(10), 2325–2338. <https://doi.org/10.1177/0003702817721527>